Scale Dependence and Localization of the Deformation of Arctic Sea Ice

David Marsan, Harry Stern, Ron Lindsay, Jérôme Weiss

Scale Dependence and Localization of the Deformation of Arctic Sea Ice

David Marsan
Laboratoire de Géophysique Interne et Tectonophysique, Université de Savoie, France

Harry Stern and Ron Lindsay
Polar Science Center, Applied Physics Laboratory, University of Washington, Seattle, Washington, USA

Jérôme Weiss
Laboratoire de Glaciologie et Géophysique de l'Environnement, Observatoire de Grenoble, Grenoble, France
(Received 7 November 2003; published 20 October 2004)

A scaling analysis of the deformation of Arctic sea ice over a 3-day time period is performed for scales of 10 to 1000 km. The deformation field is derived from satellite radar data; it allows us to study how a very large solid body—the Arctic sea-ice cover—deforms under the action of heterogeneous forcing winds and ocean currents. The deformation is strongly localized at small scales, and can be characterized as multifractal. This behavior is well known for turbulent flows, and is here also observed for a deforming solid. A multiscaling extrapolation to the meter scale (laboratory scale) shows that, at the 3-day time scale, about 15% of the deformation is larger than 10^{-4} s^{-1}, implying brittle failure, over 0.2% of the total area.

DOI: 10.1103/PhysRevLett.93.178501 PACS numbers: 92.10.Rw, 05.45.Df, 62.20.Dc, 62.20.Hg

Sea-ice extends across the entire Arctic Ocean in winter with an average thickness of 2–3 m. The ice drifts under the influence of winds, currents, and internal stress gradients, producing spatial gradients in the ice velocity that we refer to as deformation. The large aspect ratio of lateral extent to thickness means that the deformation is well characterized by surface displacements. The physical and mechanical properties of saline ice are well documented at the laboratory scale [1,2] and can be considered relatively homogeneous.

Satellite data offer a unique opportunity to analyze the strain field of the deforming ice over a large range of scales, from about 10 km to the size of the Arctic basin. Previous analyses have revealed the strong heterogeneity of this strain field, leading to the definition of "linear kinematic features" [3], which account for most of the deformation, and "quasirigid plates" [4], which move as solid bodies. However, such definitions rely on arbitrary and scale-dependent strain-rate thresholds. Here, we present a scaling analysis of the strain field of the Arctic sea-ice cover: (i) how deformation depends on the observation scale, (ii) to what extent deformation is heterogeneous and localized, (iii) how this localization depends on the scale, and (iv) how the scaling can be used to extrapolate the statistics of the deformation to small scales. To our knowledge, such scaling analysis of the strain field of a deforming geophysical solid is new. As a comparison, the reconstitution of crustal deformation along major plate boundaries through global positioning system and interferometric synthetic aperture radar techniques is spatially much sparser, with historical coverage that may not be fully representative of the longer term deformation and that is only a remote signature of the deformation taking place at depth.

Sea-ice deformation is an important process in the Arctic climate system. Deformation creates openings and pressure ridges in the ice, driving changes in the ice thickness distribution, which controls the exchange of heat, moisture, and momentum between the ocean and the atmosphere. Sea-ice models have been reasonably successful at reproducing the observed mean ice motion, but less so with ice deformation [5]. Knowledge of the scaling properties of sea-ice deformation could be useful for improving model representations of sea-ice rheology.

The data for this study come from the RADARSAT Geophysical Processor System (RGPS) [6], which uses synthetic aperture radar (SAR) images from the Canadian RADARSAT satellite as input to an ice-tracking algorithm that identifies and follows over 40 000 points on the sea ice by means of a cross-correlation technique [7,8]. The tracking begins each November after freeze-up, with the points initially spaced 10 km apart, and continues until the following spring, when the onset of melt erases the distinct signatures of the surface features. The points tracked by the RGPS define the vertices of cells which are initially square (10×10 km) but which drift and deform with the ice cover. Suppose the vertices of a cell are identified in two SAR images three days apart. RGPS computes the velocities of the vertices and then the spatial velocity gradients, based on the line integrals of the velocity components around the boundary of the cell. The RGPS deformation product then consists of time series of all cell positions and their associated velocity gradients. The RGPS ice tracking is highly accurate, with error standard deviations on the order of 100 meters. Since the ice typically drifts 5–50 km over three days, velocity errors are less than 2%. This leads to errors in the velocity gradients of about 3.5% over three days [9]. We then

compute the invariants of the strain-rate tensor for each cell: the divergence and shear rates $\dot{D}$ and $\dot{S}$. Henceforth the term deformation means the quantity $\dot{\epsilon} = \sqrt{\dot{D}^2 + \dot{S}^2}$, also known as the total deformation rate.

The RGPS data provide unprecedented spatial detail of Arctic sea-ice motion and deformation, but with a complex mix of spatial and temporal information. For this study we focus on the spatial pattern of deformation at one point in time: 00:00 UTC on 6 November 1997. We search the RGPS deformation data for all cell observations spanning that time, i.e., for which the first SAR image is before that time and the second is after. There are 43 748 such cells. We then eliminate: (i) cells adjacent to the coast, which have initial size 25×25 km^2; (ii) cells for which there are more than seven days separating the two SAR images; and (iii) cells whose areas have changed by more than a factor of 2 (i.e., current area <50 km^2 or >200 km^2), which makes the calculation of deformation unreliable. After applying these three criteria we are left with 42571 cells (Fig. 1).

We wish to compute deformation over a range of spatial scales. At the smallest scale we have the deformation of each cell. At larger scales we aggregate cells as follows. Consider a box of width W centered at a certain location within the data (a "seed" point). We find all the cell centers that lie inside the box, and compute the average velocity gradients where the contribution from each cell is weighted by its area. From these large-scale gradients we compute the deformation $\dot{\epsilon}$. Assuming horizontal scaling isotropy, we define the spatial scale L as the square root of the actual area covered by the cells, which can never exceed W but is typically close to W. By changing the size of the box we obtain samples of the deformation at different scales (denoted $\dot{\epsilon}_L$). The seed points are defined on a regular grid with spacing equal to half the box size. Adjacent boxes overlap, so the samples are not all independent. If a box is not at least 50% covered by cells, that sample is discarded.

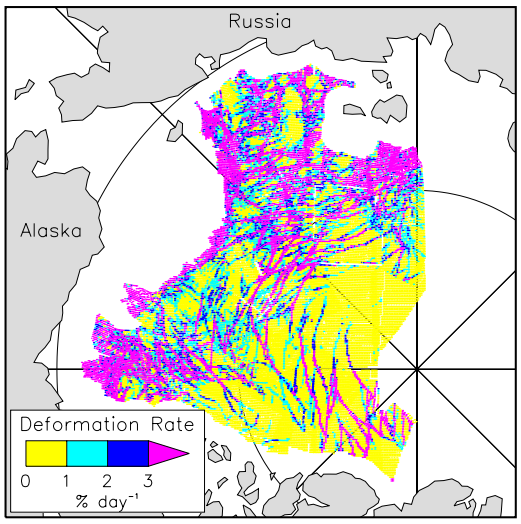

FIG. 1 (color online). Sea-ice deformation rate on 6 November 1997 from 42571 RGPS cells.

Figure 1 shows the deformation at the $L = 10$ km scale of individual cells, at which scale the localization along quasilinear structures is well pronounced. Figure 2 shows 81586 values of $\dot{\epsilon}_L$ vs L computed by our sampling procedure. Within each range of scales the mean value of deformation $\langle \dot{\epsilon}_L \rangle$ is plotted at the mean scale. The scaling $\langle \dot{\epsilon}_L \rangle \sim L^{-H}$ is observed over two decades in scale. A standard least squares fit to the mean values (gray line) gives an exponent of $H = 0.20$ with a squared correlation of 0.97. To estimate the uncertainty in H we used a bootstrap method, yielding an error standard deviation of 0.01. The value of H is robust with respect to changes in the box sizes and the number of bins.

The power-law decrease of $\langle \dot{\epsilon}_L \rangle$ with L is a signature of the spatial correlations present in the deformation field. We verified this by randomly reshuffling the velocity gradients of the RGPS cells among themselves and repeating our analysis procedures. We found a clear departure from power-law behavior. A simple argument leads to the prediction that $\langle \dot{\epsilon}_L \rangle - \langle \dot{\epsilon}_M \rangle \sim L^{-1}$ in this case, where $\langle \dot{\epsilon}_M \rangle$ is the large-scale ($\simeq$1000 km) mean for the randomly reshuffled distribution. We found this prediction to be accurate. We therefore conclude that the original $\langle \dot{\epsilon}_L \rangle \sim L^{-H}$ scaling cannot be attributed to a decay inherent in the sampling procedure, but is a result of the spatial structure in the deformation field.

In addition to the mean deformation, we investigate the scale dependence of the distribution of $\dot{\epsilon}_L$. For decreasing L the distribution is shifted toward large values (hence an increase in the mean) but also the deviation from the mean increases more rapidly than the increase in the mean itself. Equivalently, a systematic change toward shallower log-log tails of the probability density function (pdf) of $\dot{\epsilon}_L$ is observed as L decreases (Fig. 3). This enhancement of anomalously large deformation rates amounts to the strengthening of the localization at small scales. Table I shows that as the scale decreases, the largest 15% of the deformation is accommodated by a smaller portion of the sea-ice cover, and involves larger deformation rates.

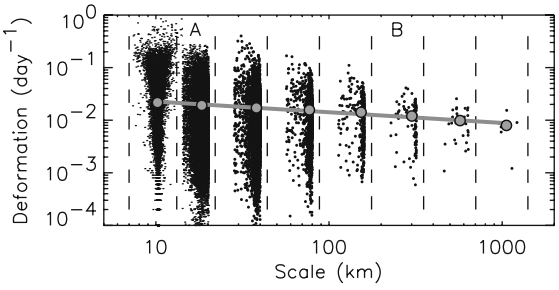

FIG. 2. Total deformation rate $\dot{\epsilon}_L$ as a function of scale L (81586 samples). Vertical dashes define bins. Gray dots are means within each bin. Gray solid line is least squares fit to mean values. *A* is 13–20 km scale; *B* is 160–320 km scale.

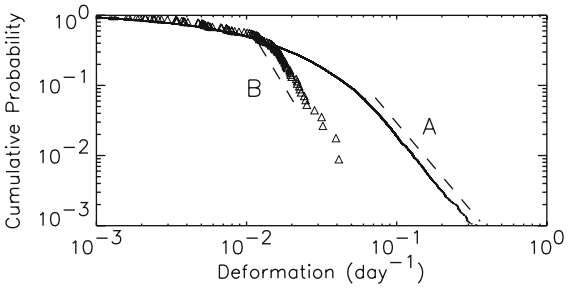

FIG. 3. Cumulative probability of observing a given deformation rate, for the 13–20 km scale (A) and the 160–320 km scale (B). Slope of dashed lines: -2.5 (A) and -3.6 (B). The slope becomes shallower as the scale decreases.

We examine the scale dependence of $\dot{\epsilon}_L$ more thoroughly by the use of a multifractal analysis, which estimates the change in the pdf f_L of $\dot{\epsilon}_L$ by computing the scaling of the moments $\langle \dot{\epsilon}_L^q \rangle$. We do this for $q > 0$ (since there are zero values in the deformation field) and $q < 3$, since a transition [10] is observed at about $q_c = 2.5$ to 3.0: the pdf f_L decays as $\dot{\epsilon}_L^{-3.5}$ for large $\dot{\epsilon}_L$ and small L, hence moments of order $q > q_c$ diverge. The moments $\langle \dot{\epsilon}_L^q \rangle$ vs L for $q = 0.5$ to 3.0 are given in Fig. 4 along with the least squares lines. Let the absolute values of the slopes be denoted by $\beta(q)$, so that $\langle \dot{\epsilon}_L^q \rangle \sim L^{-\beta(q)}$. Figure 5 shows $\beta(q)$ vs q and $\zeta(q) = q - \beta(q)$ vs q, yielding the scaling exponents of the dispersion velocity $\dot{\epsilon}_L \times L$ (by analogy with turbulence). These functions have strong curvatures, indicating multifractality of the deformation. They are remarkably well approximated by a quadratic fit $\beta(q) = aq^2 + bq$ with $a = 0.13$ and $b = 0.068$ (Fig. 5, solid curves), indicating that the total deformation can be modeled by a log-normal multiplicative cascade process (see [11] for such a model in the case of 3D fully developed turbulence). While multifractality is a well-known property of fluid flows at high Reynolds numbers, it is observed here to also occur for a deforming solid. Another description of ζ takes the form $\zeta(q) = hq - K(hq)$ where h measures the departure from nonconservation and $K(q) = C_1(q^\alpha - q)/(\alpha - 1)$ is the moment scaling function of the underlying conserved cascade [10]. We obtain $\alpha \simeq 1.95$, hence very close to the log-normal $\alpha = 2$ value, $C_1 \simeq 0.22$ and $h \simeq 0.76$. As a comparison, empirical values for 3D fully developed turbulence are $\alpha = 1.3 \pm 0.1$, $C_1 = 0.25 \pm 0.05$, and $h = 1/3$ [12].

TABLE I. Mean deformation rate $\dot{\epsilon}$, threshold $\dot{\epsilon}_{85\%}$ (85th percentile), and percentage of surface area with deformation greater than the threshold. The numbers at the 1 m scale are extrapolated from the 160–320 km scale.

Scale	Mean $\dot{\epsilon}$ (day^{-1})	$\dot{\epsilon}_{85\%}$ (day^{-1})	Surface
160–320 km	0.011	0.04	3.2%
13–20 km	0.02	0.12	1.6%
1 m	0.14	10	$\simeq 0.2\%$

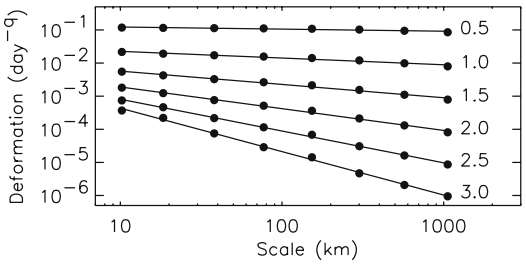

FIG. 4. Moments of the deformation rate $\langle \dot{\epsilon}_L^q \rangle$ as a function of scale L for $q = 0.5$ to 3.0, and the least squares lines. The slopes of these lines are denoted $-\beta(q)$.

Recast in terms of the dispersion of sea ice, let L be the separation of two points and r be the change in separation after three days. Then the moments of r scale as $\langle r^q \rangle \sim L^{\zeta(q)}$. Martin and Thorndike [13] obtained $\langle r^2 \rangle \sim L^{1.8}$ for a set of 12 buoys in the Bering Sea, with L in the 5–50 km range and 4-day time scale. We obtain $\zeta(2) = 1.34$ (Fig. 5) hence $\langle r^2 \rangle \sim L^{1.34}$. As with turbulence, the dispersion follows non-Gaussian statistics, hence the moments $\langle r \rangle$ and $\langle r^2 \rangle$ are not sufficient to characterize the distribution, as implied by Figs. 3 and 5.

In material science, strain rate is a key parameter controlling the nature of the mechanisms that accommodate the deformation [14]. The strain-rate ranges corresponding to each of these mechanisms are deduced from laboratory experiments. For saline ice, a transition between ductile behavior (dislocation related) and brittle failure is observed under compressive loading around 10^{-4} s^{-1} ($\simeq$10 day^{-1}) [2]. Because of the scaling nature of the sea-ice strain-rate field, nothing can be directly deduced about small-scale deformation mechanisms from our strain-rate estimates at the scale of 10 km or above. However, one possibility is to use the present multifractal analysis to extrapolate the distribution of the total deformation rate to the 1 m scale, which is close to the size of samples studied in the laboratory and is also close to the characteristic thickness of sea ice. This approach is based on the assumption that the scaling relationship observed between 10 and 1000 km also characterizes the subresolution scales down to 1 m. Scaling analyses of sea-ice fracture patterns as seen in satellite and aerial images argue for such scale invariance within this scale range [15,16].

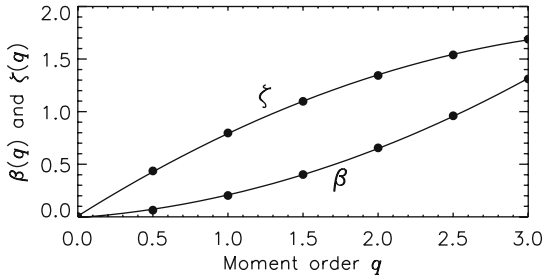

FIG. 5. Functions $\beta(q)$ and $\zeta(q) = q - \beta(q)$ vs moment order q (circles) and the best-fit quadratic curves.

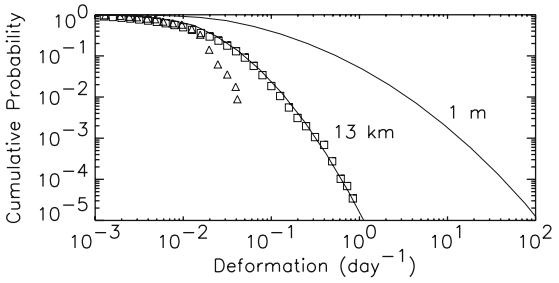

FIG. 6. Cumulative probability of observing a given deformation rate, extrapolated to scales 13 and 1 m (curves), from the probability distribution of the total deformation at the 160–320 km scale (triangles). For comparison, the observed distribution at scale 13–20 km is also shown (squares).

The pdf f_2 of $\dot{\epsilon}_L$ at scale L_2 is obtained from the pdf f_1 at scale L_1 by a convolution $f_2(\dot{\epsilon}) = \int d\gamma \lambda^{-c(\gamma)-\gamma} \times f_1(\lambda^{-\gamma}\dot{\epsilon})$ where λ is the scale ratio L_1/L_2, γ is the order of singularity, and $c(\gamma)$ is the codimension function obtained from $\beta(q)$, by a Legendre transform [17] when $\lambda \gg 1$, yielding $c(\gamma) = \max_q\{q\gamma - \beta(q)\}$, or by a more involved inversion procedure otherwise. For $\lambda \gg 1$, we model $c(\gamma)$ as a quadratic function $c(\gamma) = [(\gamma - b)^2/4a]$, for γ between b and $2q_c a + b$ (corresponding to the interval $0 < q < q_c$), the lower bound implying that the very small values of $\dot{\epsilon}_L$ are badly constrained in this extrapolation. The cumulative probabilities at $L =$ 13 km and $L = 1$ m, extrapolated from the pdf of $\dot{\epsilon}_L$ at $L =$ 160–320 km, are shown in Fig. 6. At 1 m, about 15% of the deformation is accommodated in the brittle (>10 day^{-1}) regime, corresponding to 0.2% of the sea-ice surface area (Table I). These numbers are representative of the 3-day time scale over which the deformation field is sampled. For shorter durations, intermittency of the deformation, as indicated by the occurrence of ice-quakes [18] or observed with stress gauges [19], implies that the localization should increase, with the possibility that most of the deformation could be accommodated by brittle failure over short, transient fracturing episodes involving very localized structures.

To conclude, we have found that: (i) the mean deformation of sea ice is related to the spatial scale of observation according to a power law with exponent -0.20. Similar analyses performed at the 3-day scale for other dates in the 1997–1998 winter yield similar values (-0.22 ± 0.05). Also, a more local (200×200 km^2, with 5 km resolution) analysis over a whole year gave a mean winter (October to July) exponent of -0.18. The mean summer (July to mid-September) exponent is -0.45, close to the oceanic dispersion exponent (estimated at about -0.4 from [13]), which is consistent with a deformation regime closer to free drift. Turbulence theory predicts a $L^{1/3}$ velocity scaling, hence a $-2/3$ value for this exponent. Compared to pure free drift at the ocean surface, the exponent observed during the Arctic winter is significantly smaller (in magnitude), hence the localization of deformation is significantly less. This suggests that the winter cover responds to the heterogeneity of the forcing by attenuating the spatial variability imposed by the latter. (ii) The deformation is log-normally multifractal. Hence the small-scale deformation can be statistically related to larger scales, for example, in downscaling sea-ice model outputs. (iii) The deformation becomes more and more localized at smaller scales, with highly deforming structures occupying a smaller fraction of the total area. (iv) The predicted deformation rates at small scales could imply that most of the deformation is brittle.

This work was supported by CNRS, the NASA Cryospheric Sciences Program, and the NSF International Opportunities for Scientists and Engineers. We thank R. Kwok and the RGPS team at JPL for providing the data.

[1] D. M. Cole, Eng. Fract. Mech. **68**, 1797 (2001).
[2] E. M. Schulson, Eng. Fract. Mech. **68**, 1839 (2001).
[3] R. Kwok, in *IUTAM Symposium on Scaling Laws in Ice Mechanics and Ice Dynamics* (Kluwer, Dordrecht, 2001), p. 315.
[4] R. E. Moritz and H. L. Stern, in *IUTAM Symposium on Scaling Laws in Ice Mechanics and Ice Dynamics* (Kluwer, Dordrecht, 2001), p. 335.
[5] R.W. Lindsay, J. Zhang, and D. A. Rothrock, Atmosphere-Ocean **41**, 35 (2003).
[6] Data from four winters are available on the RGPS web site at www-radar.jpl.nasa.gov/rgps/radarsat.html
[7] M. Fily and D. A. Rothrock, IEEE Trans. Geosci. Remote Sensing **25**, 570 (1987).
[8] R. Kwok, in *Analysis of SAR Data of the Polar Oceans*, edited by C. Tsatsoulis and R. Kwok (Springer-Verlag, Berlin, 1998), p. 235.
[9] R.W. Lindsay and H. L. Stern, J. Atmos. Ocean. Technol. **20**, 1333 (2003).
[10] D. Schertzer and S. Lovejoy, J. Geophys. Res. **92**, 9693 (1987).
[11] A. M. Yaglom, Sov. Phys. Dokl. **2**, 26 (1966).
[12] F. Schmitt, D. Lavallée, D. Schertzer, and S. Lovejoy, Phys. Rev. Lett. **68**, 305 (1992).
[13] S. Martin and A. S. Thorndike, J. Geophys. Res. **90**, 7223 (1985).
[14] M. F. Ashby, Acta Metall. **20**, 887 (1972).
[15] T. Falco, F. Francis, S. Lovejoy, D. Schertzer, B. Kerman, and M. Drinkwater, IEEE Trans. Geosci. Remote Sensing **34**, 906 (1996).
[16] J. Weiss, Surv. Geophys. **24**, 185 (2003).
[17] G. Parisi and U. Frisch, in *Turbulence and Predictability in Geophysical Fluid Dynamics and Climate Dynamics*, edited by M. Ghil, R. Benzi, and G. Parisi (Italian Physical Society, North-Holland, 1985), p. 84.
[18] Y.V. Dudko, H. Schmidt, K. von der Heydt, and E. K. Scheer, J. Geophys. Res. **103**, 21775 (1998).
[19] J. K. Lewis and J. A. Richter-Menge, J. Geophys. Res. **103**, 21831 (1998).